Strong magnetophonon resonance induced triple G-mode splitting in graphene on graphite probed by micromagneto Raman spectroscopy

Caiyu Qiu,[1,*] Xiaonan Shen,[1,*] Bingchen Cao,[1] Chunxiao Cong,[1] Riichiro Saito,[2] Jingjiang Yu,[3] Mildred S. Dresselhaus,[4,5] and Ting Yu[1,6,7,†]

[1]*Division of Physics and Applied Physics, School of Mathematical and Physical Science,*
Nanyang Technological University, 637371, Singapore
[2]*Department of Physics, Tohoku University, Sendai, Miyagi 9808578, Japan*
[3]*Nanotechnology Measurements Division, Agilent Technologies, Inc., Chandler, Arizona 85226, USA*
[4]*Department of Electrical Engineering and Computer Science, Massachusetts Institute of Technology,*
Cambridge, Massachusetts 02139-4037, USA
[5]*Department of Physics, Massachusetts Institute of Technology, Cambridge, Massachusetts 02139-4037, USA*
[6]*Department of Physics, Faculty of Science, National University of Singapore, 117542, Singapore*
[7]*Graphene Research Centre, National University of Singapore, 117546, Singapore*

The resonance between the G-band phonon excitation and Landau level optical transitions in graphene has been systematically studied by micromagneto Raman mapping. In purely decoupled graphene regions on a graphite substrate, eight traces of anticrossing spectral features with G-mode peaks are observed as a function of magnetic fields up to 9 T, and these traces correspond to either symmetric or asymmetric Landau level transitions. Three distinct split peaks of the G mode, named G_-, G_i, and G_+, are observed at the strong magnetophonon resonance condition corresponding to a magnetic field of $\sim$4.65 T. These three special modes are attributed to (i) the coupling between the G phonon and the magneto-optical transitions, which is responsible for G_+ and G_- and can be well described by the two coupled mode model and (ii) the magnetic field-dependent oscillation of the G_i band, which is currently explained by the G band of graphite modified by the interaction with G_+ and G_-. The pronounced interaction between Dirac fermions and phonons demonstrates a dramatically small Landau level width ($\sim$1.3 meV), which is a signature of the ultrahigh quality graphene obtained on the surface of graphite.

I. INTRODUCTION

As a novel two-dimensional (2D) carbon material, graphene possesses many extraordinary properties owing to the charge carriers moving like massless Dirac fermions.[1] When the Dirac fermions in graphene are subjected to a magnetic field, the quantized energies, which are called Landau levels (LLs) with Landau index n, will form. An ultrahigh-quality graphene sample is crucial for many fundamental physics studies in graphene. Specifically, the high quality of graphene samples can be reflected by the long lifetime of the Dirac fermions and the narrow spectral widths of the LLs.[2]

For evaluating the in-plane crystal size, the defects, and the degree of decoupling, the LL spectral width can be compared using different measurement techniques, such as magneto-Raman spectroscopy,[2,3] infrared spectroscopy,[4,5] scanning tunneling spectroscopy (STS),[6–8] and cyclotron resonance.[9] For these measurements, they used pure graphene sheets that were found to be decoupled from the graphite substrate due to the twist angle between the layers[10] or became physically detached from the Bernal-stacked layers underneath[11,12] (hereafter, we call this structure "graphene on graphite"),[2,3,6,9] or epitaxial few-layer graphene grown on SiC.[5,8] For example, using infrared spectroscopy, the LL spectral width of mechanically exfoliated graphene on a Si/SiO$_2$ substrate is about 40 meV[4] and of the non-Bernal stacked $\sim$100 layers of epitaxial graphene on SiC is between 4 meV (at $B = 60$ mT) and 10 meV (at $B = 4$ T).[5] However, using STS, the LL widths of the decoupled graphene on graphite and in epitaxial graphene were found to be $\sim$10 meV[6] and $\sim$1.5 meV,[8] respectively.

Here, we obtain the LL width by Raman spectroscopy measurements.

Raman spectroscopy is a nondestructive technique used at ambient pressure, which has been widely applied to characterize nanocarbon materials[13–17] and to probe materials under different environments or modifications, including their exposure to an external magnetic field.[18–22] The physics of graphene in the presence of magnetic fields can also be studied by the magneto-Raman technique.[2,3,23–25] Specifically, when the transition energy of the inter-LL electronic excitations (i.e., magnetoexcitons) matches the energy of the G-band phonon, magnetophonon resonance (MPR) will occur.[26] The MPR in graphene has been theoretically predicted to have a fine structure and anticrossing behavior for the Raman G mode.[23,24] Recently, several experiments have observed the MPR effect for different types of graphene samples.[2,3,25] In multilayer epitaxial graphene, one of the two components of the Raman G band shows clear variations in both frequency and width as a function of magnetic field.[25] Comparisons of the MPR measurements with the theoretical models gave a LL width of 90 cm^{-1} ($\sim$10 meV). Yan *et al.*[2] identified graphenelike regions that are electronically decoupled from the host graphite after scanning a Kish graphite sample with a spatial resolution of $\sim$80 μm. From these regions, they observed a more pronounced Dirac-like MPR effect over a range of magnetic fields centered at 5 T. The sharper resonance than observed in previous results was attributed to the smaller LL level transition width of 26 cm^{-1} ($\sim$3 meV). Soon thereafter, Faugeras *et al.*[3] also identified graphenelike domains on natural graphite with

a much higher spatial resolution (~ 1 μm) by micro-Raman mapping in magnetic fields up to 32 T. They also found the LL width to be 25 cm^{-1} ($\sim$3 meV) for 2.8 T. However, in order to discuss the coupling of LL transitions with G-band spectral phonons, the LL width should be comparable to the intrinsic spectral width of the G band ($\sim$10 cm^{-1} = 1 meV), which requires graphene samples of much higher quality than those that were used in earlier work.

In this work, micromagneto Raman spectroscopy possessing a 2D mapping function with $\sim$1 μm spatial resolution is used to quickly distinguish domains of graphene with different extents of decoupling from the graphite. In a specifically decoupled graphene region formed during the mechanical exfoliation process, we have observed detailed information on the mixing of the G-band phonon and the Dirac fermion magnetoexcitons by a high-resolution magnetoresonant Raman measurement with a LL spectral width as sharp as 10.6 cm^{-1} ($\sim$1.3 meV). Eight LL transitions are observed revealing LL crossing of the G mode with an anticrossing behavior due to both symmetric and asymmetric LL transitions. In particular, for the $n = -2$ to 1 LL transition, the Raman G peak is found to split into three unambiguous peaks (G_-, G_i, and G_+) over a certain range of magnetic fields around $B \sim 4.65$ T, which has been proposed to exist[2] but failed to be resolved previously because of the broadening of the LL spectral width. From the behavior of the three resolved peaks as a function of magnetic field, we can discuss the coupling of the G-band phonon and the LL transitions quantitively by using theoretical models. In particular, a new feature, which is proposed in this paper by the coupling of graphene magnetoexciton phonons and phonons of the graphite substrate, is fully investigated by a driven harmonic oscillator model. Thus, the LL spectra studied by this technique can give access to important many-body effects for graphene and other 2D materials.

II. EXPERIMENT

Graphite samples ($\sim$100 μm) were exfoliated from single-crystal natural graphite and transferred onto a silicon wafer with an insulating layer of 300-nm SiO$_2$. To observe the Raman spectra of the graphite sample at low temperature ($\sim$5 K) and in magnetic fields up to 9 T, a customer-designed confocal magneto-Raman mapping system was set up (see Fig. 1).

A monomode optical fiber with a 5 μm core was used to introduce the solid-state excited incident light (Nd:YAG, 532-nm wavelength) with $\sim$5-mW laser power onto the sample. The laser beam was focused by a 50 $\times$ objective lens into a region of 1 μm in diameter under the optimized ray path in the system. The scattered light was collected by a multimode optical fiber with a 50-μm core in the backscattering geometry. The collected scattered light was measured by a spectrometer grating of 1800/mm equipped with a thermoelectrically cooled (207 K) charge-coupled device detector. In our experiments, the excitation beam and the collected signal were not circularly polarized so that signals from the two different configurations (cocircular and cross circular) could be obtained at the same time.

The samples were placed inside a vacuum stick, which was pumped to $\sim$10^{-5} mbar pressure and then filled with 20-mbar He gas before immersion in a cryostat filled with
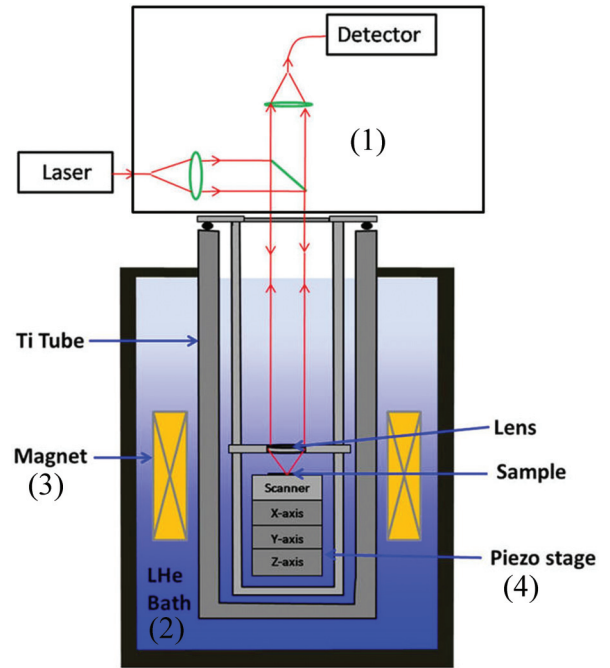

FIG. 1. (Color online) Schematic drawing of our experimental setup. The customer designed confocal magneto-Raman mapping system mainly contains the following parts: (1) the backscattering configuration Raman system; (2) the cryostat that can provide a liquid helium (LHe) bath; (3) the superconducting magnet mounted inside the cryostat to provide a magnetic field perpendicular to the sample; and (4) the nonmagnetic *X-Y-Z* piezo stage for mounting the tested sample.

liquid helium. A superconducting magnet, which was mounted inside the cryostat, applied magnetic fields up to 9 T in steps of 0.1 T in the direction perpendicular to the sample plane. Nonmagnetic piezo stages, consisting of *X-Y-Z* positioners and *X-Y* scanners, allowed Raman imaging over dimensions up to 30 $\times$ 30 μm^2 with $\sim$1-μm spatial resolution. Our magneto-Raman measurements were performed at 5 K.

A commercial atomic force microscope (AFM) system (Agilent 5500) equipped with an environmental chamber was used to find the decoupled graphene domains within the top layer of graphene. In order to reduce the disturbance of an adsorbed water layer on the graphene surfaces and thus to enhance the detection sensitivity, all AFM measurements were performed under a low relative humidity level of $\sim$11% ($\pm$1%), which was established and maintained by placing a saturated salt solution of lithium chloride into the sealed environmental chamber. The samples were characterized in the acoustic ac mode with MikroMasch DPE14 probes that typically have a resonance frequency of 160 kHz and a force constant of 5.7 N/m.

III. EXPERIMENTAL RESULTS AND DISCUSSION

We measured the magnetic field dependence of the G phonon mode for several exfoliated graphite samples. The optical image and related information of a group of tested graphite samples are shown in Fig. 2. In this paper, we will take the graphite on the left side in Fig. 2(a) [enclosed by a solid black line in Fig. 2(a)] as a representative example.
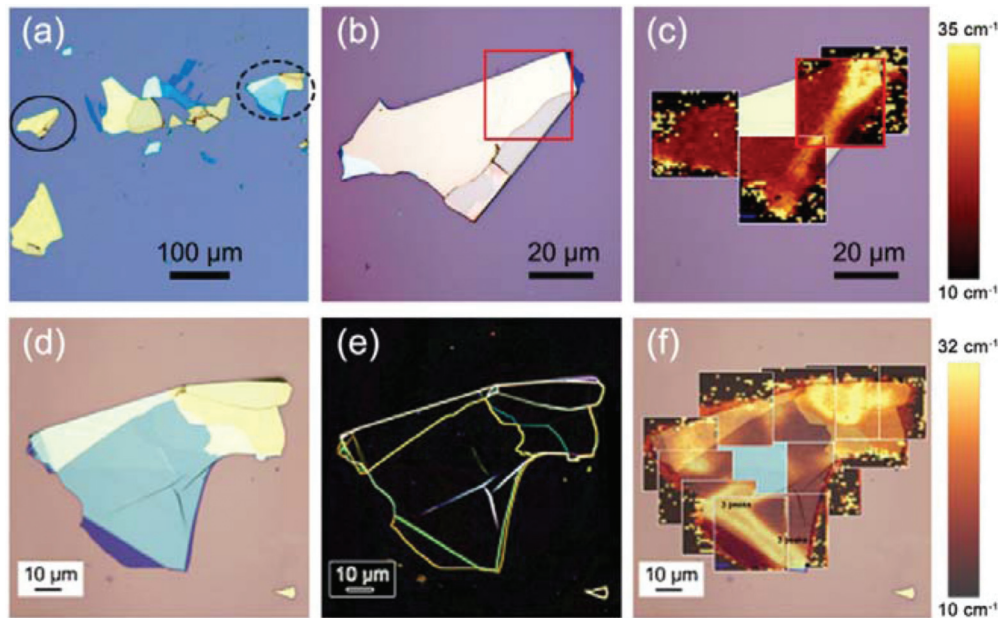
FIG. 2. (Color online) The tested graphite samples with strong MPR regions. (a) Optical image of several graphite samples on a Si/SiO$_2$ substrate at 50× magnification. Among these samples, two graphite flakes show MPR phenomenon, which are circled by solid and dashed black lines. (b) Enlarged optical image of the graphite sample enclosed in a solid line in (a). The MPR effect studied in the main text is observed in the area highlighted by a red square. (c) Raman images of the G-band width at $B = 4.8$ T stacks with the optical image and the color scale for the spectral width of the G band is shown on the right. (d) Original and (e) "glowing edge" filter applied optical images of the graphite sample highlighted by the dashed circle line in (a). (f) Raman images of the G-band width at $B = 4.8$ T are pieced together according to the optical image underneath the graphite flake shown in (d).
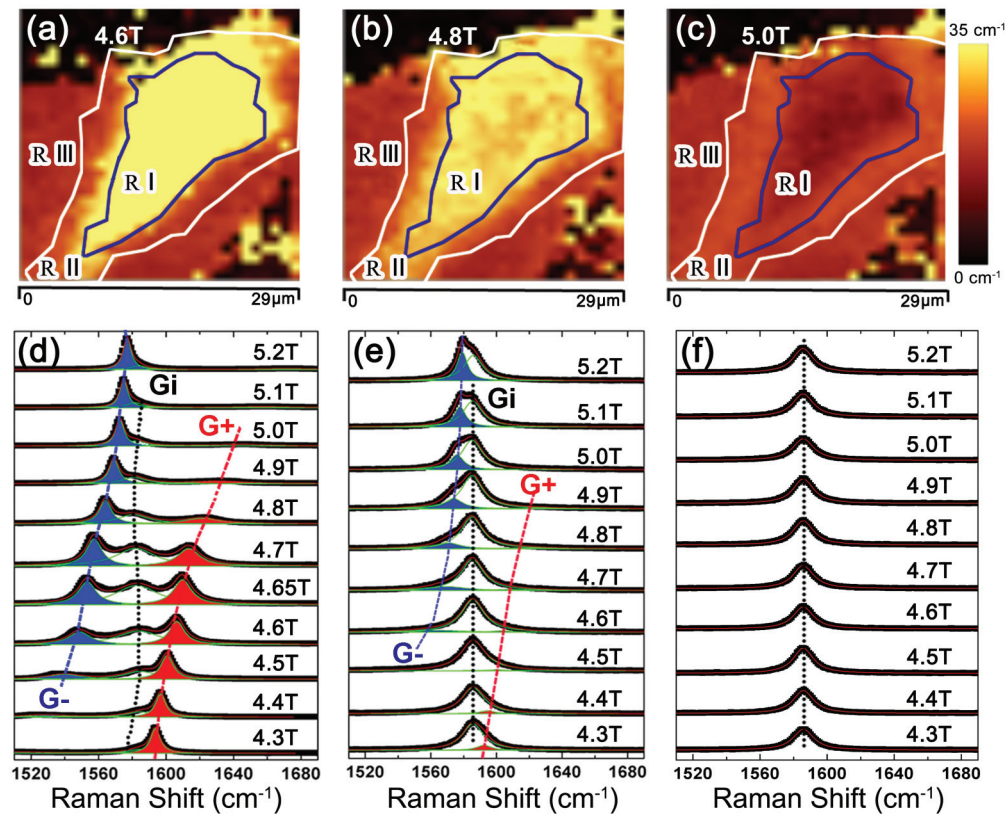

FIG. 3. (Color online) (a)–(c) Raman images of the G-band spectral width at $B = 4.6$, 4.8, and 5.0 T. The blue and white lines separate the scanned sample area into three different regions (marked as R I, R II, and R III) in which the evolutions of the G-peak frequency with magnetic field are different. (d)–(f) The evolution of the Raman spectra under a B field from 4.3–5.2 T for the sample regions of (d) R I, (e) R II, and (f) R III. Dashed lines in (d)–(f) are guides to the eyes.

Note that the experimental results can be reproduced in other samples. Figures 3(a)–3(c) present Raman images of the G-band spectral width from the selected graphite surface at $B = 4.6$, 4.8, and 5.0 T, respectively. According to the image contrast, we divide the area into three regions with their boundaries drawn by blue and white lines, where three types of distinctive behaviors in the G band can be found.

In Figs. 3(d)–3(f), we present the detailed evolutions of Raman spectra in R I, R II, and R III with magnetic fields from 4.3 to 5.2 T, where the optical absorptions between the two almost degenerate LLs, from $n = -2$ to 1 and from $n = -1$ to 2 (denoted by $L_{-2,1}^{-1,2}$), are resonant with the G phonon (see Fig. 4). In the case of R I [Fig. 3(d)], the G-band spectra at 4.3 T can be deconvoluted into three Lorentzian peaks, which

are labeled G_-, G_i, and G_+ according to their vibrational frequencies. The weak satellite peak (G_- mode) around 1520 cm^{-1} at 4.3 T gradually blueshifts and increases its intensity as it approaches the resonant magnetic field of 4.65 T. When the magnetic field is higher than 4.65 T, the G_+ mode starts to move away from the G_i mode and shows a rapid decrease in intensity. On the other hand, in R II [Fig. 3(e)], although the intensity of the G_- mode is large for $B > 4.8$ T and displays a clear mixing with the G_i mode, the G_+ mode intensity is weak and appears only as a shoulderlike subpeak with a large spectral width. In the other region outside the white line [R III, Fig. 3(f)], the G band does not exhibit obvious changes from 0–9 T, which is consistent with the previous report.[2] The different degrees of MPR can also be evaluated by the maximum G-band widths: ~ 85 cm^{-1} in R I, ~ 70 cm^{-1} in R II at 4.65 T, and ~ 14 cm^{-1} in R III.

In Fig. 4(a), the magneto-Raman spectra are plotted as a function of magnetic field for the region R I. The Raman intensities are shown by a color scale, where eight distinct lines of LL transitions cross with a horizontal line that corresponds to the G-band phonon energy at ~ 1580 cm^{-1} (=0.196 eV).

First, we consider the origin of these magnetic field-dependent features observed in Fig. 4(a). Following the analysis in Ref. 3, these traces are associated with the inter-LL transitions of Dirac fermions and belong to two different series [Fig. 4(b)]. One series is the $L_{-n,n}$ series [dotted black lines in Fig. 4(a)] originating from the symmetric inter-LL transitions from $-n$ to n, which can be detected using the excitation/detection light in the cocircular polarization configurations (σ^-/σ^- and σ^+/σ^+). They are assigned to be purely electronic excitations and are expected to be the most pronounced inter-LL features.[27] On the other hand, the $L_{-(n+1),n}^{-n,n+1}$ series [red and blue lines in Fig. 4(a)] are attributed to the asymmetric transitions coming from cross-circular polarization configurations (σ^-/σ^+ and σ^+/σ^-), which lead to the MPR effect emphasized in this work. The most pronounced MPR, caused by the $L_{-2,1}^{-1,2}$ transition around 4.65 T, will be theoretically simulated and discussed later in this paper, and the curves fitted by theory are presented as the dashed red and blue lines for the G_+ and G_- bands, respectively. Moreover, the LL transitions $L_{-5,4}^{-4,5}$ and $L_{-4,4}$, which cross the G band at the low magnetic fields of 1.5 and 1.7 T, respectively, have been observed here, too. For this assignment of LL transitions, the resonant fields at which the traces cross the G line can be calculated (see Appendix A). The calculated values for the resonant magnetic field B_r agree with the observed crossing magnetic fields, in which the Fermi velocity v_F in this sample is fitted to be $(1.04 \pm 0.01) \times 10^6$ m/s.

Next, we will quantitatively interpret the G_+ and G_- modes in terms of the two coupled mode model previously proposed by Goerbig *et al.*[23] and Yan *et al.*[2] It has been proposed that the G_+ and G_- features are mixtures of the phonon and the LL transition, which can be described by[2]
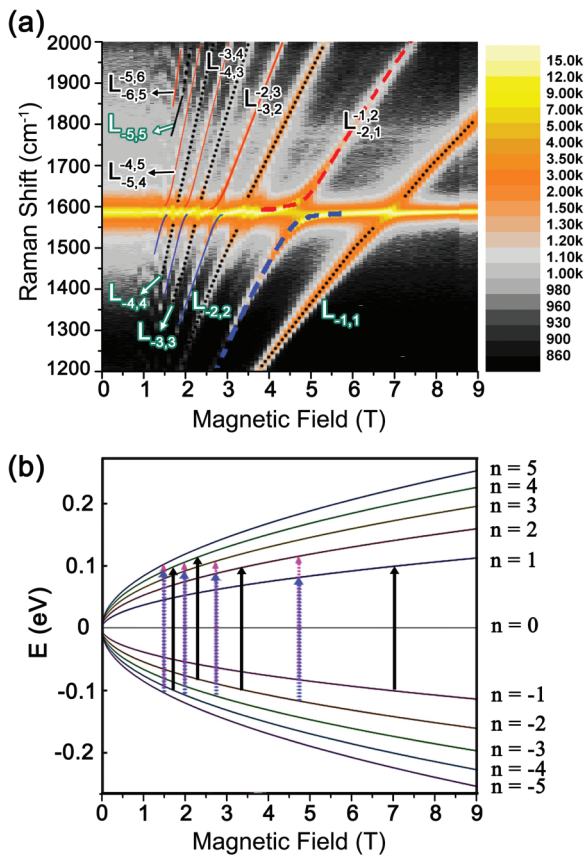
(a)

(b)

FIG. 4. (Color online) (a) Color scale map of the Raman spectra as a function of magnetic field taken from sample region R I. In (a) the black dotted lines provide guidance for the observed symmetric LL excitations $L_{-n,n}$ (from $-n$ to n); red and blue lines represent the asymmetric LL transitions $L_{-(n+1),n}^{-n,n+1}$. The dashed red and blue lines around 4.7 T are simulated curves as discussed below. (b) The schematic diagram of the Landau energies of monolayer graphene as a function of magnetic field. Vertical lines indicate various LL transitions that couple to the G-band phonon with the energy of 0.196 eV. The dashed red and dashed blue lines stand for the $L_{-(n+1),n}^{-n,n+1}$ transitions from $-n$ to $n + 1$ (response to the cross-circular polarization configuration σ^+/σ^-) and from $-(n + 1)$ to n (response to the cross-circular polarization configuration σ^-/σ^+), respectively. The black lines represent the $L_{-n,n}$ transitions (response to the cocircular polarization configurations σ^-/σ^- and σ^+/σ^+).

$$\tilde{\omega}_\pm(B) = \frac{\omega_G + \Omega(B)}{2} + i\frac{\gamma_G + \gamma_\Omega}{2}$$
$$\pm \sqrt{\left(\frac{\omega_G - \Omega(B) + i(\gamma_G - \gamma_\Omega)}{2}\right)^2 + g(B)^2},$$

$$(1)$$

TABLE I. Parameters obtained by us compared with those reported by previous works. NA means that the data values are not given.

Technique and reference	Sample type	v_F (10^6m/s)	Coupling strength g (cm^{-1})	γ_G (cm^{-1})	γ_Ω (cm^{-1})	τ (fs)
B-Raman, this work	Graphene on graphite	1.04	28.6	2.5	10.6 @4.65 T	460
B-Raman, Yan *et al.* (Ref. 2)	Graphene on graphite	1.03	37	2	26 @4.7 T	200
B-Raman, Faugeras *et al.* (Ref. 25)	Epitaxial graphene (∼70 layers)	1.02	26	2	90 Constant	54
B-Infrared, Kim *et al.* (Ref. 4)	Monolayer graphene	1.18	NA	NA	161 @6.3 T	30
B-Infrared, Faugeras *et al.* (Ref. 5)	Epitaxial graphene (∼100 layers)	1.02	NA	NA	80 @4 T	60
B-STS, Li *et al.* (Ref. 6)	Graphene on graphite	0.79	NA	NA	32.3 @4 T	150
B-STS, Miller *et al.* (Ref. 8)	Epitaxial graphene (∼10 layers)	1.13	NA	NA	12.1 @5 T	400

where the real and the imaginary parts of $\tilde{\omega}_\pm$ give the energy and the half width at half maximum intensity of these two modes, respectively, while ω_G and $\Omega(B)$ denote the energies of the G-band phonon and the LL transition. Here, γ_G and γ_Ω are introduced as the broadening parameters, representing, respectively, the half widths of the G phonon and the LL transition, and $g(B)$ is the magnetic field-dependent coupling strength, being proportional to $\sqrt{B}$ so that $g(B) = c\sqrt{B}$. Determined by the experimental data, we can obtain the parameters at $B = B_r$ (see Appendix B). The calculated values are the G phonon width $\gamma_G = 2.5$ cm^{-1}, the LL transition half width $\gamma_\Omega(B_r) = 10.6$ cm^{-1} (∼1.3 meV), a constant coefficient $c = 13.27$ cm^{-1}/T$^{1/2}$, and the coupling strength $g(B_r) = 28.6$ cm^{-1}. These derived values as well as the Fermi velocity v_F are compared with earlier research results by listing them in Table I. The value obtained here for γ_Ω is much smaller than previous values (26 cm^{-1}),[2,25] which is also discussed in the Introduction. The uncertainty relationship between γ_Ω and a characteristic scattering time $\tau = \hbar/\gamma_\Omega$ yields $\tau = 0.46$ ps, which is comparable to or larger than the previous report (0.4 ps) obtained by STS measurements.[8] Since the LL broadening γ_Ω is relevant to the disorder, the narrow spectral width indicates that we used a high-quality graphene or graphite sample for our measurements.

Substituting for all the determined parameters into Eq. (1), we can obtain $\tilde{\omega}_\pm$ as a function of B when using a constant value of $\gamma_\Omega(B_r)$ [see Eq. (B3)]. When the magnetic field is in the MPR region and for coupled modes with strong intensities, good agreement between the simulated curves and the experimental data points is achieved for both the phonon energy and the full width at half maximum [(FWHM); see illustration in Appendix B]. However, we found that the model does not fit the data well when the magnetic field is away from resonance. This indicates that the two coupled mode model is appropriate at the resonance and becomes a worse approximation away from resonance, where other resonances will give a significant contribution to the electron-phonon coupling.

Note that the LL spectral width in graphene does change with the magnetic field as observed in far-infrared transmission experiments.[5] To improve the fitting for the off-resonance region and to provide an empirical set of parameters working over a wide magnetic field range, we adjust γ_Ω as a function of magnetic field B according to an ad hoc functional form:

$$\gamma_\Omega(B) = G_O\left(1 + \frac{1}{A(B - B_r)^2 + A_1}\right)^{-1} + A_2(B - B_r). \tag{2}$$

The first term of the B dependence of γ_Ω given in Eq. (2) comes from the experimental fact that the sum of the spectral widths for $\tilde{\omega}_+$ and $\tilde{\omega}_-$ becomes a minimum at $B = B_r = 4.65$ T. The second term of Eq. (2) is an additional magnetic field dependence of the spectral width of the intrinsic LL transition, which should vanish at $B = B_r$.

Substituting the expression for $\gamma_\Omega(B)$ given by Eq. (2) and allowing γ_G to be a constant, the real and imaginary parts of $\tilde{\omega}_\pm(B)$ then have five fitting parameters: G_O, A, A_1, A_2, and γ_G. The fitted parameters to the experimental data are $G_O = 16.5$ cm^{-1}, $A = 50.0$, $A_1 = 2.3$, $A_2 = 1.6$, and $\gamma_G = 1.6$ cm^{-1}. $\gamma_\Omega(B)$ is drawn in Fig. 5(a) using the right side scale (solid squares), which shows a minimum γ_Ω value at $B = B_r$. When we use Eq. (2), both the peak frequencies and widths, respectively, of the G_+ and G_- modes over the larger magnetic field range of 3 to 7 T now can be fitted very well by the theoretical curves as shown in Figs. 5(a) and 5(b). Under this modified model, the G-band phonon half linewidth γ_G is found to be 1.6 cm^{-1} (i.e., FWHM is 3.2 cm^{-1}), and the LL transition half width at resonance is modified to be 11.5 cm^{-1} (∼1.4 meV). It should be noted that the obtained γ_G does not mean the spectral width of the G band for the off-resonance region in $B \sim 3$ T or $B \sim 7$ T in Fig. 5(b), where the FWHM gives about (7.8 ± 0.5) cm^{-1}. This deviation occurs because the other LL transitions are crossing the G phonon mode around $B \sim 3$ T or $B \sim 7$ T [see Fig. 4(a)], which makes the width of the G phonon mode broad.
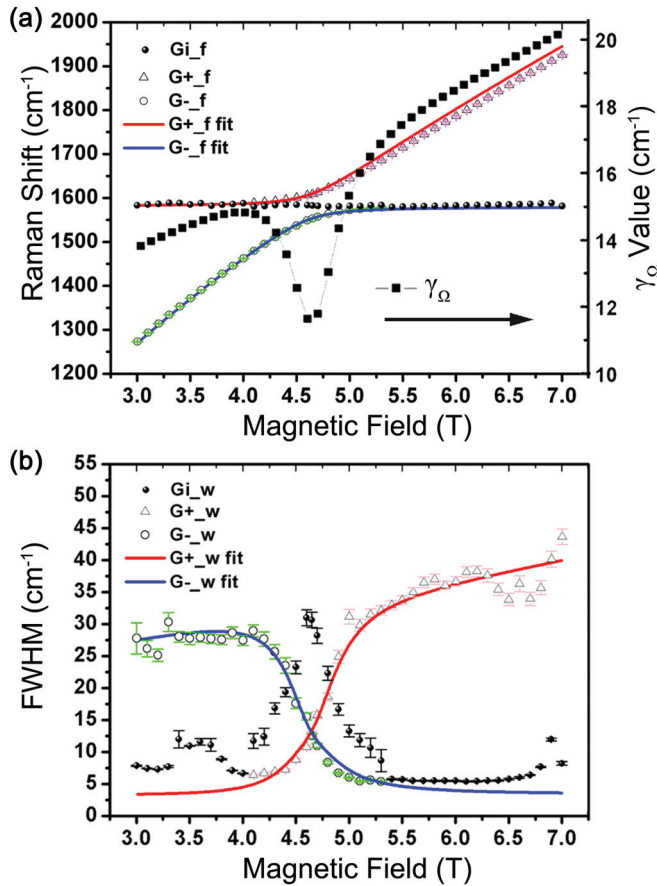
FIG. 5. (Color online) The theoretical fits by the two coupled mode model with a B-dependent γ_Ω for (a) the energy $\tilde{\omega}_\pm$ in Eq. (1) and (b) the FWHM of the G_+ and G_- modes. The red branch corresponds to the G_+ mode and the blue branch represents the G_- mode. The error bars of the experimental values for the G_+ mode are drawn in pink color, while for the G_- mode they are drawn in green color. γ_Ω as a function of B used for fitting the model to our experimental results is presented in (a). The data points for the G_i mode are also shown by black dots. Note: f and w represent frequency and linewidth, respectively.

In fact, Ando[24] calculated the self-energy of the G-band phonon, where the imaginary part (spectral width) becomes a maximum at $B = B_r$. Although the behavior of $\tilde{\omega}_+$ and $\tilde{\omega}_-$ can be explained by the self-energy calculation,[24] the resonance region around $B = B_r$ in which both $\tilde{\omega}_+$ and $\tilde{\omega}_-$ appear for a given B cannot be explained. Thus, we adopted the two coupled mode model and applied the model with modified γ_Ω for describing the experimental results in a broader B region. In the two coupled mode model, the two peaks appear around $B = B_r$, and the spectral width of each $\tilde{\omega}_+$ or $\tilde{\omega}_-$ is defined. If we compare the spectral width of the two coupled modes with that of the self-energy, we should read the width of the overall peak profile of the G phonon, or alternatively measure the frequency difference of G_+ and G_- by $\tilde{\omega}_+ - \tilde{\omega}_-$ as the spectral width of the G phonon, which reaches a maximum value at $B = B_r$, showing mutual agreement between the two models. It is also noticed that γ_Ω shows a minimum value at $B = B_r$, which is somehow unexpected since we presume that the lifetime of the magnetoexciton should be shorter at $B = B_r$ as it is for the G-band phonon. To exploit the physical picture of Eq. (2), further study is needed and will be a problem to be solved in the future. Nevertheless, this field-dependent γ_Ω suggests that other effects might need to be considered in the "two coupled mode model" and such reconsideration should bring new fundamental physics into the understanding of the phonon-magnetoexcitons interaction.

We now briefly discuss the overall features of the Raman signal from R I in the close vicinity of the G-band phonon frequency (1580 cm^{-1}), and we mainly focus on the behavior at each $B = B_r$. First, the frequency positions of the three G peaks (G_-, G_i, G_+) displayed in Fig. 6(a) show a series of anticrossing behaviors between G_+ and G_- each time the MPR occurs. Besides the main MPR near $B_r = 4.65$ T, the coexistence of the three split peaks can be observed at each MPR for asymmetric LL transitions at a magnetic field range from 1.5 to 4.65 T. In addition, the response of the G phonon to the $L_{-n,n}$ (symmetric) LL transitions is weaker than that to the $L_{-(n+1),n}^{-n,n+1}$ (asymmetric) LL transitions, with a less distinct avoided crossing around the resonant magnetic field B value. The reason is that the $L_{-(n+1),n}^{-n,n+1}$ transitions have the symmetry of the representation E_2, while the $L_{-n,n}$ transitions have the symmetry of the representation A_2, allowing the former to couple to the E_{2g} optical G-band phonon more effectively and thus leading to a stronger MPR coupling.[27] Second, at each resonant magnetic field, two coupled modes G_+ and G_- always have the same FWHM intensity [Fig. 6(b)], which is consistent with the two coupled mode model.[2] Third, the sum of the integrated intensities of the three G modes displayed in Fig. 6(c) reaches a maximum at $B = B_r$. Phonon generation and the LL transitions (electronic excitations) contribute to the Raman signal at $B = B_r$. Thus, the total Raman intensity achieves a maximum, because the energy denominator for the time-dependent perturbation for the two processes has a minimum at resonance, even though the contribution of G_+ or G_- to the total intensity does not show a maximum at $B = B_r$.

Now, we ask the simple questions: (1) what is the origin of G_i and (2) why is the G_i intensity enhanced at $B = B_r$? In order to answer these questions, let us now pay attention to the behavior of the G_i mode, which shows a set of well-pronounced maxima in their linewidths at $B = B_r$ as shown in Fig. 6(b). When the G_+ or G_- modes appear near every resonant magnetic field, the intensity of the G_i mode will drop down [Fig. 6(c)]. If we look into the detailed evolution of the three modes around the main MPR magnetic field range, we can see a local maximum intensity of the G_i mode right at $B = B_r$ [Fig. 6(d)]. As for the G_i mode frequency, a weak oscillatory behavior as a function of B is noticed in this work. The oscillation of the G_i mode frequency was also observed and explained in a previous work, as the coexistence of the regions in magnetic field when using a big laser spot of 80 μm, and two distinct lifetimes were found in these works.[2] The G_i mode was previously interpreted as originating from graphene regions in which the electron lifetime is relatively short. This interpretation apparently does not work for our data, since the spatial resolution of our system is only 1 μm. Here, we would like to reconsider the interpretation of the G_i mode by
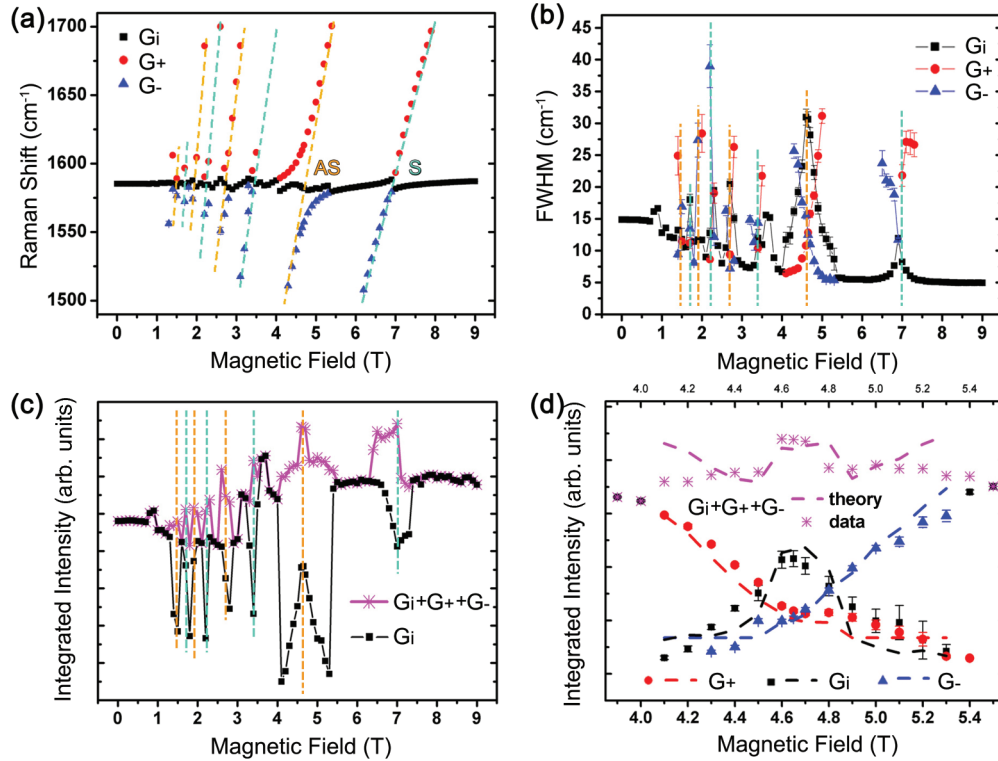
FIG. 6. (Color online) The detailed evolution of the fitted (a) frequency and (b) FWHM of the E_{2g} phonon as a function of the B field, including the middle frequency mode G_i (black squares) and the two coupled modes G_+ (red dots) and G_- (blue triangles). The labels S and AS denote, respectively, symmetric $L_{-n,n}$ (cyan dashed lines) and asymmetric $L_{-(n+1),n}^{-n,n+1}$ LL transitions (orange dashed lines). (c) The sum of the intensities (integrated total area, indicated by pink stars) of the three G bands and the intensity evolution of the G_i mode (black squares) as a function of magnetic field. The solid lines are guides to the eyes. (d) The zoom-in view of the sum and individual intensity variation of the three G modes around the main MPR magnetic field range. The dashed lines are theoretical fitting results that are presented using Eq. (5).

examining the magnetic field-dependent oscillatory behavior of the G_i mode in more detail.

The fluctuations of the G_i mode in the three different regions (R I, II, and III) of graphite are compared and presented in Fig. 7. Note that in this figure, the stronger the coupling is between graphene and the graphite substrate in a given region of the sample, the larger the amplitude of the variations of G_i is in both the frequency of this mode and the corresponding FWHM. In particular, in R III the graphite G peak shows almost no change under a magnetic field. Thus, the oscillation of the G_i mode in Fig. 7 is relevant to the decoupled graphene regions, where a strong LL absorption occurs.

Here, we propose a theoretical model to interpret the evolution of the width and intensity of the G_i mode, which is identified with the G peak coming from the graphite substrate. In this model, we expect the G phonon of graphite to be excited by many G-band phonons from graphene by a resonance effect between the phonon of graphene and the phonon of graphite. The coupling between G_i and the two coupled modes (G_+ and G_- of graphene) leads to an oscillation in the overall Raman intensity of the G_i peak through a driven harmonic oscillator. The variation of the intensities of the G_+ and G_- modes behaves as externally applied forces with spectral functions A_ω and B_ω, respectively, in Eq. (3), which could effectively affect the oscillatory behavior of the overall G band, and thus affect the amplitude and frequency of the G_i phonon mode. Then, we can express the equation describing the amplitude q

of the G-band vibration as follows:

$$\ddot{q} + \gamma_{Gi}\dot{q} + \omega_0^2 q = \int a A_\omega e^{-i\omega t} d\omega + \int b B_\omega e^{-i\omega t} d\omega, \quad (3)$$

where A_ω and B_ω are, respectively, the amplitudes of the G_+ mode and the G_- mode. The coefficients a and b are, respectively, introduced into Eq. (3) to characterize the coupling constant between G_i and the G_+ and G_- modes. Here, ω_0 and γ_{Gi} are, respectively, the fitting parameters of the frequency and the spectral width of the G_i peak. Since A_ω and B_ω should have the dimensions of an amplitude, they can be considered, respectively, to be equal to the square root of the peak intensities of $I(\omega_+)$ and $I(\omega_-)$ for the G_+ and G_- modes as a function of magnetic field, by using the experimental peak intensities: $A_\omega = \sqrt{I(\omega_+)}$; $B_\omega = \sqrt{I(\omega_-)}$.

Solving the differential Eq. (3) using the Fourier transform $Q = \int_{-\infty}^{+\infty} q e^{i\omega t} dt$, we can obtain the equation for the amplitude of the overall G mode:

$$Q = \frac{2\pi(a A_\omega + b B_\omega)}{(\omega_0^2 - \omega^2) + i\omega\gamma_{G_i}}. \quad (4)$$

Then, the total spectral intensity can be calculated by

$$I(\omega) = |Q|^2 = \frac{4\pi^2(a A_\omega + b B_\omega)^2}{(\omega_0^2 - \omega^2)^2 + \omega^2\gamma_{G_i}^2}. \quad (5)$$

We now fit the parameters a, b, ω_0, and γ_{G_i} to experimental measurements in the prominent MPR region around
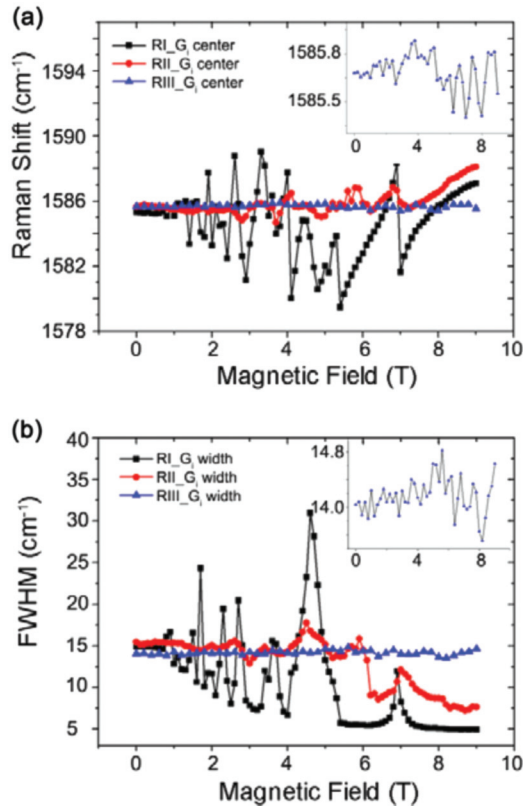
FIG. 7. (Color online) The fluctuation of the middle G_i mode in three different regions of graphite. (a) Evolution of the G_i peak center with B fields in the three representative regions on the graphite substrate. (b) Fitted FWHM of the G_i modes in these three locations as a function of magnetic field. The inset is an enlarged view of the curve taken from R III.

FIG. 8. (Color online) (a) The magnetic field dependence of the coefficients a and b in Eq. (5) used for the calculation of $I(\omega)$. (b) The fitted Raman frequency and (c) the fitted FWHM of the middle Lorentzian component of the calculated $I(\omega)$ curve (red symbols) by Eq. (5) and the corresponding values of the experimental G_i (black symbols) as a function of the magnetic B field.

$B_r = 4.65$ T. From Fig. 5(a), we can see that around the MPR region, when the magnetic field is away from B_r, the absolute value of the frequency difference between the G_+ mode (ω_+) and the averaged G_i mode ($\bar{\omega}_i \approx 1582$ cm^{-1}) is inversely proportional to the absolute value of the frequency difference between the G_- mode (ω_-) and $\bar{\omega}_i$. In contrast, for magnetic fields close to the MPR point, the frequency differences between these modes are almost the same. We postulate that the driving forces exerted by the G_+/G_- modes are related to the frequency deviation from the average frequency of the G_i mode. Therefore, for the magnetic fields in the range $B = 4.6$–4.8 T, which are close to the resonance, because $|\omega_+ - \bar{\omega}_i| = |\omega_- - \bar{\omega}_i|$, we set $a = b = 1$. When away from the resonance condition, for smaller values of the magnetic field $B < 4.6$ T, we set $a = 1, b = \frac{|\omega_+ - \bar{\omega}_i|}{|\omega_- - \bar{\omega}_i|}$. In contrast, for larger magnetic fields $B > 4.8$ T, $a = \frac{|\omega_- - \bar{\omega}_i|}{|\omega_+ - \bar{\omega}_i|}, b = 1$. The resulting evolution of a and b with magnetic fields is shown in Fig. 8(a). Consequently, at $B_r = 4.65$ T, $a = b = 1$. In accordance with this formulation, the optimized fitting of $I(\omega)$ to the experimental spectrum at 4.65 T follows Eq. (5) so that ω_0 and γ_{G_i} are, thus, found to be $\omega_0 = 1582.0$ cm^{-1}, $\gamma_{G_i} = 28.5$ cm^{-1}, which are reasonable approximations for these parameters, also subject to further examination for consistency, as discussed below. Meanwhile, a scale factor of $s = 6 \times 10^7$ is used to bring
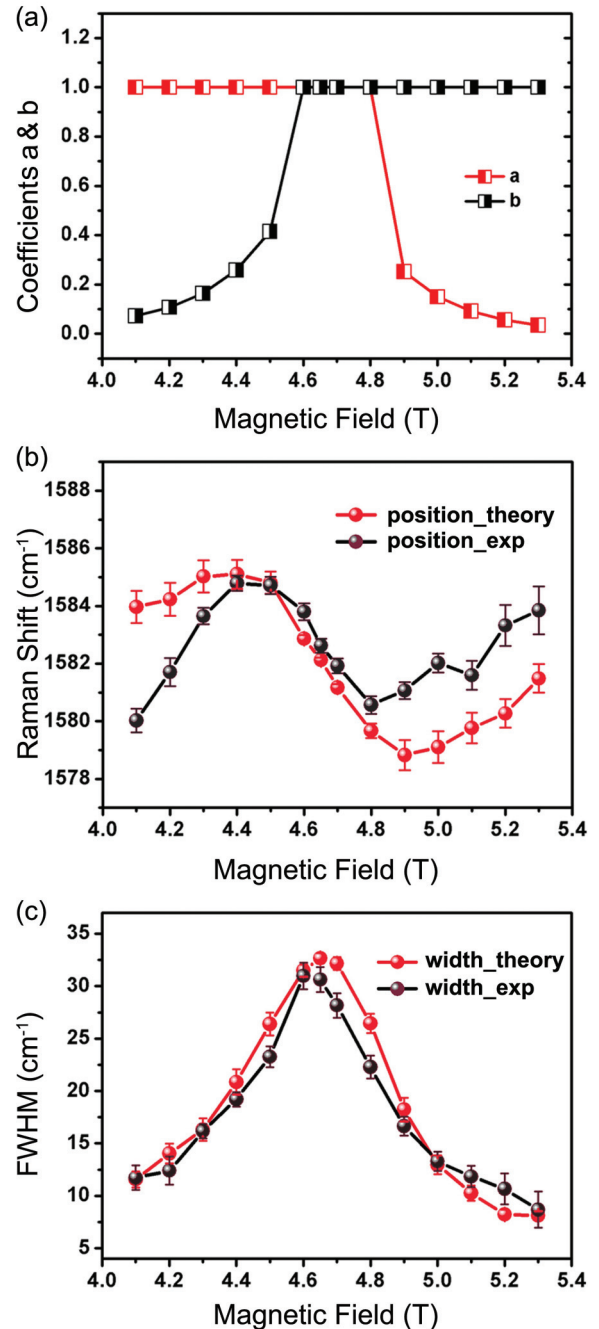
$I(\omega)$ into the same order of magnitude as the experimental spectrum.

Using the parameters determined above, the Raman spectral $I(\omega)$ curves for many B field values from 4.1–5.3 T can be calculated, and the results are plotted in Fig. 9(b). It is important to note that the highest intensities for G_+ ($B = 4.1$ T) and G_- ($B = 5.3$ T) are not at resonance ($B = B_r = 4.65$ T), and this experimental finding can be reproduced by the present
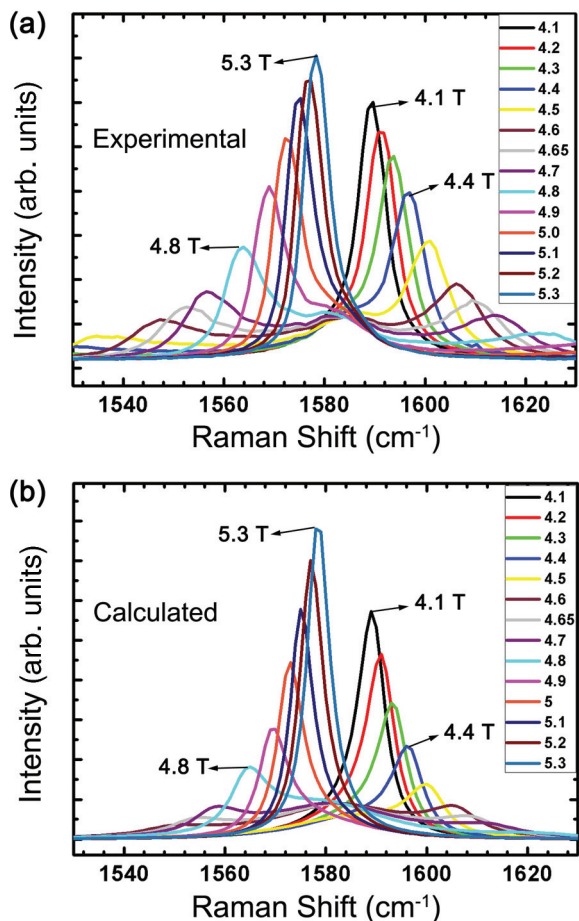
FIG. 9. (Color online) (a) Evolution of the measured Raman spectra with B fields ranging from 4.1 to 5.3 T. (b) Evolution of the simulated $I(\omega)$ curves with B fields in the same range of magnetic fields as (a). The intensities of the $I(\omega)$ curves are scaled so that the intensity of the curve at 5.3 T is the same as that of the experimental Raman spectrum at 5.3 T.

model. The overall behavior with magnetic field agrees fairly well between the simulated results and the experimental measurements.

Furthermore, a Lorentzian fitting procedure was applied to the calculated $I(\omega)$ curves in Fig. 9(b), as in the analysis of the measured Raman spectra, where each curve was deconvoluted into three Lorentzian components. Focusing on the G_i mode

in the experiments, we compared its peak position and peak width to those of the experimental G_i mode. As presented in Figs. 8(b) and 8(c), these peak features of the G_i mode can be well reproduced by this simulation model. Additionally, we fitted the peak intensities for the calculated $I(\omega)$ curves and compared them to the experimental results, including the separation of $I(\omega)$ into three modes (G_+, G_-, and G_i) and the sum of the intensities of $G_+ + G_- + G_i$ to the experimental results, as shown in Fig. 6(d). The main evolution of these intensities is consistent with that obtained from the measured Raman spectra. The reasonable fitting of the experiments and theory testifies to the validity of this model and the parameters of the model thus obtained.

The magnetoexciton-mediated interaction between phonons in graphene and graphite may be a special phenomenon found only in this graphene on graphite system. We expect some special optical processes to be operative among the magnetoexcitons, the phonons in graphene, and the metallic energy band in graphite. These processes should be the subject of future theoretical work, which will extend the knowledge of the Raman mechanism in terms of the interactions among photons, phonons, and electrons.

The successful interpretation of these features in terms of the massless Dirac fermion model and the two coupled mode model suggests the presence of a decoupled monolayer graphene sitting on the graphite surface. By the AFM technique, the graphene on graphite assumption can be further validated. The AFM topographic image [Fig. 10(b)] shows clear ridge structures on the surface of the graphite sample near region R I (red arrow). The presence of such defects favors the formation of characteristic graphene on graphite structures.[6,28,29] In epitaxial few-layer graphene grown on SiC, a distinct ridgelike network of defects formed from the out-of-plane distortions of the hexagonal graphene lattice was observed, which results in the formation of Moiré patterns clearly seen in atomically resolved scanning tunneling microscopy images.[28,29] For natural graphite, the surface is usually inhomogeneous and presents a variety of defects as well. By low-temperature STS experiments, in the region separated by a macroscopic ridgelike defect, single-layer graphene flakes decoupled from the surface of highly oriented pyrolitic graphite have been found.[6] The situation should be similar in our natural graphite sample or the Kish graphite studied by others.[2]
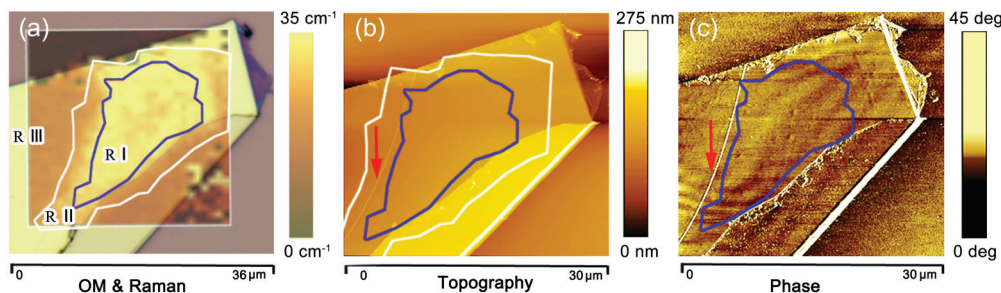

FIG. 10. (Color online) (a) Comparing the Raman image of the G-band spectral width at $B = 4.8$ T, labeling the three regions as in Fig. 1(b), with the optical microscope (OM) image. (b) AFM height image and (c) AFM phase signals image of the tested graphite sample. A ridge defect structure on the surface near the MPR region is clearly revealed and indicated by the red arrows in (b) and (c). Clear phase contrast is captured in (c), with a tilted pattern that is resolved in the region enclosed by the blue outline in (c).

It has been verified and demonstrated by many research groups that phase contrast in the ac AFM mode imaging is very sensitive to the relative change of properties relative to the averaged value, such as the mechanical (stiffness, friction) and adhesive properties.[30] As a consequence, the phase imaging shown in Fig. 10(c) could serve as another experimental means for us to distinguish those decoupled graphene domains from the nondecoupled parts of the sample. Figure 10(c) shows the simultaneously acquired phase signal of MPR locations on this graphite sample, where a ridge structure near region R I is also clearly resolved (red arrow). Furthermore, despite some surface contamination, stripe contrasts are observed on the graphite surface, and a stripe pattern tilted from the stripe pattern on graphite (R III) is clearly resolved in the region R I enclosed by the blue outline in Fig. 10(c). Both the location and orientation of the phase pattern are matching well with the identified strong MPR region R I in the corresponding Raman mapping shown in Fig. 10(a). In this regard, we infer that the varied MPR strength [Figs. 3(d) and 3(e)] in R I and R II is linked to the degree of decoupling in the graphene layers. This interpretation is reasonable considering that R II is adjacent to both R I and R III.

IV. CONCLUSIONS

Here, we report low-temperature (∼5 K) magneto-Raman measurements on bulk graphite samples in a magnetic field (B) up to 9 T. Several graphene on graphite areas were distinguished by Raman imaging and further confirmed by the AFM technique. We have demonstrated rich MPR effects, which are due to the coupling of the G phonon and the electronic excitations between Dirac fermion LLs. The two coupled mode model together with our simulation model successfully explain the main features observed in the splitting of the G phonon into G_+, G_-, and G_i modes. The experimental behavior of the middle frequency mode (G_i) is reproduced by a physical model that the G-band of the graphite substrate is resonant with the G_+ and G_- bands. The present results show a phonon-phonon interaction between the decoupled graphene layer and the graphite substrate mediated by magnetoexcitons. The appearance of eight obvious features are identified with the crossing of the G-band phonon with LLs, including one occurring at a magnetic field as low as 1.5 T. The narrow LL width of 10.6 cm^{-1} (∼1.3 meV) in the MPR provides evidence for the high quality of the decoupled graphene regions of the sample that show a unique strong electron-phonon interaction, allowing study of the magnetoexciton interaction between the optical phonon and the inter-LL electronic transitions in monolayer graphene. The especially high quality of the graphene layer found here also implies the important effect of the substrate on the quality of the graphene samples, which will inspire future work to achieve high-quality graphene layers and other 2D materials for both fundamental and applied studies.

APPENDIX A: CALCULATION OF THE LLs OF DIRAC FERMIONS AND MPR MAGNETIC FIELDS

The resonance field for each of the eight LL crossings shown in Fig. 4 can be estimated quite precisely. These LL crossings are the main subject of this paper. The calculation of the resonance magnetic fields for these eight crossings is shown below. For massless relativistic electrons in monolayer graphene, the energy dispersion is linearly dependent on the momentum as $E = \upsilon_F \hbar k$, and the energy of the LL scales with magnetic field as $\sqrt{B}$ and with the Landau index n as

$$E_n = \text{sign}(n)\sqrt{2n}\frac{\hbar \upsilon_F}{l_B}, \tag{A1}$$

where υ_F is the Fermi velocity at the Dirac point for our sample, and $l_B = (\frac{\hbar c}{B|e|})^{1/2} = \frac{25.66}{\sqrt{B}}$nm is the magnetic length.

The electron-phonon coupling results in a series of discrete features, which correspond to the resonances in the traces we observed. When an optically active inter-LL transition (magnetoexciton) is tuned to be resonant with the E_{2g} optical phonon energy, the coupling effect is strongly enhanced. This resonant coupling is the so-called MPR. As a result, the resonant magnetic fields will satisfy the MPR condition that the energy spacing between properly selected LLs of Dirac fermions coincides with the energy of the G phonon excitation at ∼196 meV.

According to the selection rule, two series of excitations can be observed by Raman spectroscopy: $L_{-(n+1),n}^{-n,n+1}$ with $\Delta |n| = \pm 1$ (optical-like excitations, right- and left-hand circular polarization) and $L_{-n,n}$ with $\Delta |n| = 0$. Then, we have

for $L_{-(n+1),n}^{-n,n+1}$, $\Delta E_n = (\sqrt{n} + \sqrt{n+1})\sqrt{2}\hbar \upsilon_F \left(\frac{\sqrt{B}}{25.66}\text{nm}\right)$

$$= 196 \text{ meV}, \tag{A2}$$

TABLE II. The observed resonance fields B_r compared with the theoretical prediction.

No.	1	2	3	4	5	6	7	8
Observed	1.50 T	1.70 T	2.00 T	2.30 T	2.70 T	3.40 T	4.65 T	7.00 T
Calculated	1.51 T	1.70 T	1.95 T	2.26 T	2.74 T	3.40 T	4.65 T	6.79 T
	−5 → 4		−4→3		−3→2		−2→1	
LL Transitions		−4→4		−3→3		−2→2		−1→1
	−4→5		−3→4		−2→3		−1→2	

Magnetic field		ω_+	ω_-	$\omega_+ - \omega_-$
4.6 T	Peak position (cm^{-1})	1606.35	1548.82	57.53
	FWHM (cm^{-1})	10.78	15.55	–
4.65 T	Peak position (cm^{-1})	1609.68	1553.30	56.38
	FWHM (cm^{-1})	12.84	12.50	–
4.7 T	Peak position (cm^{-1})	1613.43	1557.39	56.04
	FWHM (cm^{-1})	15.79	11.00	–

For $L_{-n,n}$, $\Delta E_n = (2\sqrt{n})\sqrt{2}\hbar\upsilon_F\left(\dfrac{\sqrt{B}}{25.66}nm\right)$

$$= 196 \text{ meV}. \tag{A3}$$

where B is a dimensionless value when the value of B is taken in unit of tesla. For a given n, the resonant magnetic field is calculated by Eqs. (A2) and (A3).

This determines the Fermi velocity υ_F to be $(1.04 \pm 0.01) \times 10^6$ m/s by fitting to the observed B_r values. All of the crossing magnetic fields B for the eight different transitions discussed in this paper are in excellent agreement with the measured values for the resonant magnetic field seen from this graphitic flake (Table II).

APPENDIX B: THE SIMULATION BY THE TWO COUPLED MODE MODEL USING CONSTANT γ_Ω

Table III lists the Raman spectra parameters and Fig. 11 shows the theoretical fittings.

At the resonance magnetic field B_r, which is defined by $\omega_G = \Omega(B_r)$, Eq. (1) is simplified as

$$\tilde{\omega}_\pm(B_r) = \omega_G + i\frac{\gamma_G + \gamma_\Omega}{2} \pm \sqrt{g(B_r)^2 - \left(\frac{\gamma_G - \gamma_\Omega}{2}\right)^2}.$$

This equation indicates that at $B = B_r$, we expect $\tilde{\omega}_+$ and $\tilde{\omega}_-$ to have an equally weighted superposition of the

phonon and the magnetoexciton. Thus, the G_+ and G_- spectral features may have the same FWHM $\gamma_G + \gamma_\Omega$, and the frequency difference between G_+ and G_- becomes $2\sqrt{g(B_r)^2 - (\frac{\gamma_G - \gamma_\Omega}{2})^2}$.

Since the resonant B field is about 4.65 T, the energy splitting and the width of the two coupled modes at resonance can be calculated by averaging the parameters obtained at 4.6, 4.65, and 4.7 T. By averaging the six FWHM values, we have $\gamma_G + \gamma_\Omega = 13.08$ cm^{-1}.

By averaging the splitting at 4.6, 4.65, and 4.7 T, we have

$$2\sqrt{g(B_r)^2 - \left(\frac{\gamma_G - \gamma_\Omega}{2}\right)^2} = 56.65 \ cm^{-1}.$$

By averaging the G-band frequencies for G_+, G_-, we obtain $\omega_G = 1581.50$ cm^{-1}.

At a large magnetic field, the LLs are discrete. Thus, the G-band linewidth is expected to become sharp because of the much reduced electron and phonon coupling. The smallest G phonon width in our experiment is $\sim$4.95 cm^{-1} at 9 T in Fig. 8(b), which corresponds to $2\gamma_G$. Therefore, $\gamma_G = 4.95$ $cm^{-1}/2 = 2.47$ cm^{-1}. Hence, the LL transition half width at resonance: $\gamma_\Omega(B_r) = 10.61$ cm^{-1}. Based on these values and Eq. (2) in the main text, we have that at resonance, $g(B_r) = 28.62$ $cm^{-1} = c^*\sqrt{4.65 \text{ T}}$, $c = 13.27$ $cm^{-1}/T^{1/2}$. Then, we get

$$g(B) = 13.27^*\sqrt{B}. \tag{B1}$$

As for the energy of the LL transition $L_{-2,1}^{-1,2}$, which is defined as $\Omega_{-2,1}^{-1,2}$, we have the expression:

$$\Omega_{-2,1}^{-1,2} = (\sqrt{1} + \sqrt{2})\sqrt{2}\hbar\upsilon_F\left(\frac{\sqrt{B}}{25.66}nm\right)$$

$$= (733.92\sqrt{B})\,cm^{-1} \quad (\upsilon_F = 1.04 \times 10^6 \text{ m/s}). \tag{B2}$$
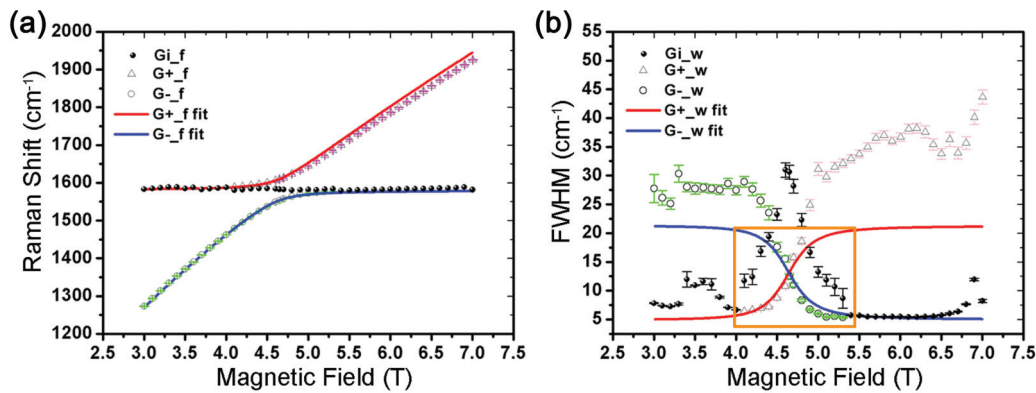

FIG. 11. (Color online) The theoretical fittings of (a) the frequency and (b) the FWHM intensity obtained by using the two coupled mode model when using constant γ_Ω [Eq. (B3)]. The red branch corresponds to the G_+ mode, and the blue branch represents the G_- mode. The experimental data points of the G_i mode are also shown here by black dots. When the magnetic field is in the MPR region and for the coupled modes with strong intensities, the simulated curves match well with the experimental data points. Note: f and w represent frequency and linewidth, respectively.

Substituting the calculated values and the Eqs. (B1) and (B2) determined above into Eq. (1) in the main text, we can then fit the frequency and widths at various magnetic fields by taking the real or imaginary part of

$$\omega_\pm = \frac{1581.50 + 733.92\sqrt{B}}{2} + \frac{10.61 + 2.47}{2}i \pm \sqrt{\left[\frac{(733.92\sqrt{B} - 1581.50) + (10.61 - 2.47)i}{2}\right]^2 + (13.27\sqrt{B})^2} \ \text{cm}^{-1}.$$

(B3)

Furthermore, a similar theoretical calculation is applied to get the related parameters in R II. The half width of the LL transition is found to be 21.3 cm^{-1} ($\sim$2.6 meV), and the coupling strength is 21.2 cm^{-1}. Therefore, we speculate that the smaller coupling strength and especially the broader LL width are responsible for the weaker MPR effect in R II.

*These authors contributed equally to this work.

†Corresponding author: yuting@ntu.edu.sg

[1] A. H. C. Neto, F. Guinea, N. M. R. Peres, K. S. Novoselov, and A. K. Geim, Rev. Mod. Phys. **81**, 109 (2009).

[2] J. Yan, S. Goler, T. D. Rhone, M. Han, R. He, P. Kim, V. Pellegrini, and A. Pinczuk, Phys. Rev. Lett. **105**, 227401 (2010).

[3] C. Faugeras, M. Amado, P. Kossacki, M. Orlita, M. Kuhne, A. A. L. Nicolet, Y. I. Latyshev, and M. Potemski, Phys. Rev. Lett. **107**, 036807 (2011).

[4] Z. Jiang, E. A. Henriksen, L. C. Tung, Y.-J. Wang, M. E. Schwartz, M. Y. Han, P. Kim, and H. L. Stormer, Phys. Rev. Lett. **98**, 197403 (2007).

[5] M. Orlita, C. Faugeras, P. Plochocka, P. Neugebauer, G. Martinez, D. K. Maude, A.-L. Barra, M. Sprinkle, C. Berger, W. A. de Heer, and M. Potemski, Phys. Rev. Lett. **101**, 267601 (2008).

[6] G. Li, A. Luican, and E. Y. Andrei, Phys. Rev. Lett. **102**, 176804 (2009).

[7] E. Y. Andrei, G. Li, and X. Du, Rep. Prog. Phys. **75**, 056501 (2012).

[8] D. L. Miller, K. D. Kubista, G. M. Rutter, M. Ruan, W. A. de Heer, P. N. First, and J. A. Stroscio, Science **324**, 924 (2009).

[9] P. Neugebauer, M. Orlita, C. Faugeras, A.-L. Barra, and M. Potemski, Phys. Rev. Lett. **103**, 136403 (2009).

[10] K. Sato, R. Saito, C. Cong, T. Yu, and M. S. Dresselhaus, Phys. Rev. B **86**, 125414 (2012).

[11] J. C. Charlier, J. P. Michenaud, and P. Lambin, Phys. Rev. B **46**, 4540 (1992).

[12] J. M. B. Lopes dos Santos, N. M. R. Peres, and A. H. Castro Neto, Phys. Rev. Lett. **99**, 256802 (2007).

[13] C. Cong, T. Yu, K. Sato, J. Shang, R. Saito, G. F. Dresselhaus, and M. S. Dresselhaus, ACS Nano **5**, 8760 (2011).

[14] R. Saito, M. Hofmann, G. Dresselhaus, A. Jorio, and M. S. Dresselhaus, Adv. Phys. **60**, 413 (2011).

[15] A. C. Ferrari, Solid State Commun. **143**, 47 (2007).

[16] L. M. Malard, M. A. Pimenta, G. Dresselhaus, and M. S. Dresselhaus, Phys. Rep. **473**, 51 (2009).

[17] M. S. Dresselhaus, A. Jorio, M. Hofmann, G. Dresselhaus, and R. Saito, Nano Lett. **10**, 751 (2010).

[18] T. Yu, Z. X. Shen, Y. Shi, and J. Ding, J. Phys.: Condens. Matter **14**, L613 (2002).

[19] X. C. Dong, D. L. Fu, W. J. Fang, Y. M. Shi, P. Chen, and L. J. Li, Small **5**, 1422 (2009).

[20] Z. Q. Luo, T. Yu, Z. H. Ni, S. H. Lim, H. L. Hu, J. Z. Shang, L. Liu, Z. X. Shen, and J. Y. Lin, J. Phys. Chem. C **115**, 1422 (2011).

[21] Z. H. Ni, T. Yu, Y. H. Lu, Y. Y. Wang, Y. P. Feng, and Z. X. Shen, ACS Nano **2**, 2301 (2008).

[22] D. Yoon, H. Moon, Y.-W. Son, J. S. Choi, B. H. Park, Y. H. Cha, Y. D. Kim, and H. Cheong, Phys. Rev. B **80**, 125422 (2009).

[23] M. O. Goerbig, J.-N. Fuchs, K. Kechedzhi, and V. I. Fal'ko, Phys. Rev. Lett. **99**, 087402 (2007).

[24] T. Ando, J. Phys. Soc. Jpn. **76**, 024712 (2007).

[25] C. Faugeras, M. Amado, P. Kossacki, M. Orlita, M. Sprinkle, C. Berger, W. A. de Heer, and M. Potemski, Phys. Rev. Lett. **103**, 186803 (2009).

[26] S. Goler, J. Yan, V. Pellegrini, and A. Pinczuk, Solid State Commun. **152**, 1289 (2012).

[27] O. Kashuba and V. I. Fal'ko, Phys. Rev. B **80**, 241404(R) (2009).

[28] L. B. Biedermann, M. L. Bolen, M. A. Capano, D. Zemlyanov, and R. G. Reifenberger, Phys. Rev. B **79**, 125411 (2009).

[29] S. E. Harrison, M. A. Capano, and R. Reifenberger, Appl. Phys. Lett. **96**, 081905 (2010).

[30] R. Garcia, R. Magerle, and R. Perez, Nat. Mater. **6**, 405 (2007).